Interfacial Mass Flux at 11-Mercaptoundecanoic Acid Linked Nanoparticle Assembly on Electrodes

Jin Luo, Nancy Kariuki, Li Han, Mathew M. Maye, Laura W. Moussa, Scott R. Kowaleski, F. Louis Kirk, Maria Hepel,† and Chuan-Jian Zhong*

Department of Chemistry, State University of New York at Binghamton, Binghamton, New York 13902, and Department of Chemistry, State University of New York at Potsdam, Potsdam, New York 13676

Received: May 24, 2002; In Final Form: July 12, 2002

Thin films derived from nanocrystal cores and functionalized linkers provide a large surface area-to-volume ratio and three-dimensional ligand framework. This paper describes the results of an investigation of the interfacial mass flux and binding properties of such thin films using an electrochemical quartz crystal nanobalance technique. The hydrogen-bonding assembly from gold nanocrystals and 11-mercaptoundecanoic acid was studied as a model system. The results reveal four distinctive mass response characteristics upon pH tuning or metal ion binding. First, the protonation−deprotonation characteristic of the carboxylic acid groups in the nanostructured framework is dependent on particle core size and film thickness. Second, the pH-tunable cationic redox reaction across the electrode|film|electrolyte interface is accompanied by a large cationic electrolyte mass flux. Third, the spontaneous complexation to copper ions by the nanostructured carboxylate framework is reflected by a mass increase of the film. Fourth, the redox reaction of copper loaded in the nanostructured film is accompanied by fluxes of electrolyte cations across the electrode|film|electrolyte interface which compensate electrostatically the fixed negative charges. On the basis of the mass change detected in the presence of a series of electrolyte cations, a linear relationship was determined between the mass increase and the atomic mass of the cation, and a concurrent flux of solvent molecules was also revealed. Implications of the findings to the delineation of the design parameters of the nanostructured ligand framework for controlled release and environmental monitoring or removal of metals are also discussed.

Introduction

Nanoparticles with organic encapsulation are attractive building blocks toward responsive materials for applications in sensors, biosensors, catalysis, and controlled drug delivery.[1,2] For example, many devices or techniques for environmental monitoring of heavy metals, which threaten both human and environmental health through their increasing presence in industrial wastewater,[3,4] desire to incorporate responsive materials with large surface area-to-volume ratio and high binding specificity. Current methods are mostly based on ion-exchange chromatography involving preconcentration. Multidentate amine and carboxylate functionalities are excellent ligands for improving the selectivity,[3,5] as demonstrated using poly(L-aspartic acid) coated on an ion-exchange column[4] and self-assembled monolayers of 2,2′-thiobisethyl acetoacetate on an electrode.[6] The recent progress on synthesis, processing, and characterization of core−shell nanoparticles[1−2,7−16] has led to new opportunities to develop advanced materials with large surface area-to-volume ratio and three-dimensional ligand framework for enhancing interfacial binding sensitivity and specificity. The exploration of place-exchange reactivity[11,13] has enabled the ability to engineer shell structure with a desired functionality. The stepwise layer-by-layer method has been shown to create thin film assembly of nanoparticles of a wide variety of systems.[12,14,17,18] The exchange−cross-linking−precipitation route[19] using ω-functionalized alkanethiols and alkanethiolate-capped gold nanoparticles has provided a simple means for thin film assembly via intershell hydrogen bonding.

The viability of using multiple carboxylate sites in the assembled nanostructure as a three-dimensional ligand framework with a large surface area-to-volume ratio could provide an effective environment for binding metal ions.[20] This attribute has also been demonstrated recently for exploring carboxylate−M^{2+} binding chemistry as a bridge in constructing a multilayer assembly of nanoparticles,[17] and in solution format for colorimetric detection of metal ions.[21] Hydrogen bonding of amine and carboxylic acid groups has also been reported for assembling nanoparticles in several other systems.[22,23] Our aim of the present study is to probe in situ the interfacial mass flux and binding characteristics of the nanostructured films. The results will be very important for delineating the design parameters of chemically sensitive or responsive nanomaterials in electrochemical detection of metals and controlled release applications. Scheme 1 illustrates in a highly idealized fashion the redox reaction and possible mass fluxes at the electrode|nanostructured film|electrolyte interface. A good model system of the film can be assembled on an electrode surface by hydrogen-bonding linkage of gold nanocrystals using 11-mercaptoundecanoic acid (MUA) linker molecules.[19b,c] The understanding of the control and regulation of ion and solvent fluxes requires a quantitative correlation of the charge flow and the mass change.

The nanostructure on the electrode surface can be considered as a membrane-like film whereby electron-transfer reaction and ionic or solvent fluxes across the membrane could lead to both

* To whom correspondence should be addressed. Telephone: (607) 777-4605. E-mail: cjzhong@binghamton.edu.
† State University of New York at Potsdam.

10.1021/jp026179c CCC: $22.00
Published on Web 08/16/2002

SCHEME 1: Schematic Illustration of Possible Mass Fluxes at the Electrode|Film|Electrolyte Interface

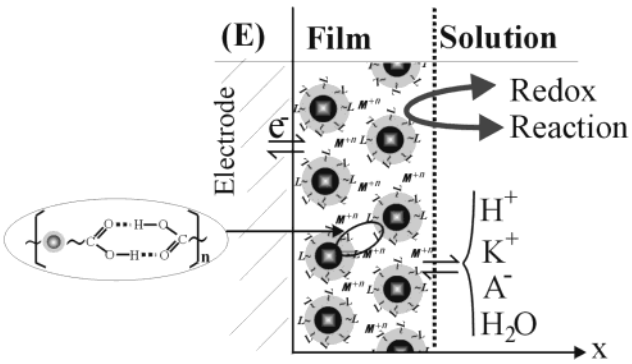

physical (e.g., swelling or deswelling) and chemical (e.g., protonation, deprotonation, or electrostatic binding) changes in the nanostructure. For self-assembled monolayers with carboxylic acid terminals, several studies[24] showed that an increase of pK_a could occur due to the decreased hydrophilicity in the two-dimensional environment. Whether such a change occurs in the nanostructured three-dimensional environment poses an intriguing question for understanding the interfacial physical and chemical phenomena of the nanostructured materials. The electrochemical quartz crystal nanobalance (EQCN) is a powerful technique to probe how ion and/or solvent fluxes respond to interfacial manipulations (e.g., pH, redox reaction) in two important ways.[25] First, it allows the correlation of the mass release/take-in with the redox potential, which is essential in sensing and controlled release applications. Second, the magnitude of the response provides a quantitative assessment of the controlled release/take-in in terms of nanoporosity, solvation, and nature of the ions. Some of these elements have recently been demonstrated for probing electrocatalysis at nanostructured catalyst interfaces.[26] In this paper, we report the results of an investigation using this technique to probe interfacial mass fluxes of nanostructured thin films at electrode surfaces, which is aimed at developing new strategies for electrochemical detection and controlled drug release[27] using nanostructured materials.

Experimental Section

Chemicals. The chemicals included decanethiol (DT, 96%), mercaptoundecanoic acid (MUA, 97%), hydrogen tetrachloroaurate ($HAuCl_4$, 99%), tetraoctylammonium bromide (TOABr, 99%), and sodium borohydride ($NaBH_4$, 99%). Solvents included toluene (99.8%), hexane (99.9%), and ethanol (99.9%). $N(CH_3)_4Cl$ was prepared from the reaction of $N(CH_3)_4OH$ and HCl. All other chemicals, LiCl, KCl, RbCl, CsCl, NH_4Cl, $Ru(NH_3)_6Cl_3$, $K_3Fe(CN)_6$, and $Cu(NO_3)_2$, were purchased from Aldrich and used as received. Water was purified with a Millipore Milli-Q water system.

Nanoparticle Synthesis. Thiolate-capped gold nanoparticles of both 2-nm (Au_{2-nm}) and 5-nm (Au_{5-nm}) core sizes were prepared in this work. The Au_{2-nm} particles were synthesized by a standard two-phase method developed by Schiffrin and co-workers[10] and a modified procedure.[11f] Briefly, $AuCl_4^-$ was first transferred from aqueous $HAuCl_4$ solution (10 mM) to toluene by phase transfer reagent TOABr (36 mM). DT was then added at a 2:1 mole ratio of DT to Au. An excess (12 times) of aqueous $NaBH_4$ was slowly added into the solution. The reaction was allowed to occur under stirring at room temperature for 4 h, producing a dark-brown solution of the DT-capped Au_{2-nm} (core size: 1.9 ± 0.7 nm). The solution was subjected to solvent removal in a rotary evaporator at room temperature and followed by multiple cleanings using ethanol and acetone.

Au_{5-nm} particles were derived from the Au_{2-nm} particles by a thermally activated processing route, the details of which were recently described.[28] Briefly, a solution of the Au_{2-nm} particles resulting from the synthesis was preconcentrated before a subsequent heating to a temperature of 140 °C, at which the core−shell structure undergoes desorption/redeposition and coalescence/growth, and eventually evolves in core size. The products, Au_{5-nm} (core size: 5.2 ± 0.3 nm), were subjected to subsequent suspension in ethanol at least three times to ensure a complete removal of solvent and byproducts. The core sizes of the nanoparticles were determined by transmission electron microscopy.[28]

Film Preparation. The preparation of the MUA-linked gold nanoparticle thin films involved a one-step exchange−cross-linking−precipitation route, the details of which were recently reported.[19b,c] Stock solutions of DT-capped Au_{5-nm} (~5 μM) or Au_{2-nm} (~100 μM) in hexane (sometimes in toluene) and MUA (5.0 mM) in ethanol were used to prepare solutions for assembling the thin film, i.e., MUA−Au_{nm}. The concentration of nanoparticles is expressed in concentration of total particles in the solution calculated using the average particle core sizes. MUA was mixed with Au_{nm} in a hexane solvent at controlled concentrations, typically in the concentration ranges of 0.1−2.0 μM for Au_{5-nm}, 1.0−10.0 μM for Au_{2-nm}, and 0.05−5.0 mM for MUA. Typical MUA to nanoparticle ratios were in the range of 50−400 to 1. The thickness of the film was controlled by the assembling time (ranging from a few hours to 1 day), which was monitored from the frequency change of the piezoelectrode. The films were thoroughly rinsed with hexane upon emersion from the assembling solution.

Substrates used for the thin film preparation included glass slides and gold film coated piezoelectrodes. The gold surfaces were cleaned by immersion in 1:3 H_2O_2 (30%)−H_2SO_4 (concentrated) solution for 3 min, and rinsed with deionized water and ethanol. (**Caution:** H_2O_2–H_2SO_4 solution reacts violently with organic compounds and should be handled with extreme care.)

Instrumentation and Measurements. An electrochemical quartz crystal nanobalance setup was employed for measurements of cyclic voltammetric curves and EQCN curves.[26,29,30] It was composed of a microcomputer controlled potentiostat (Model PS-1705, ELCHEMA) and EQCN-900 instrument (ELCHEMA). The error limit of the mass detection is less than 0.1 ng. The EQCN measurements were performed in the electrolyte solution purged with nitrogen at room temperature. All experiments were performed in three-electrode electrochemical cells. A saturated calomel electrode (SCE) was used as the reference electrode, and a Pt coil was used as the counter electrode. All electrolytic solutions were deaerated with high-purity argon or nitrogen before the measurement. All the potentials are quoted with respect to the saturated calomel electrode (SCE). QCM measurements were performed on a custom-built oscillation circuitry with sine wave output (oscillator chip Model MC12061L, Newark Electronics). The oscillator can operate in the frequency range of 2−20 MHz. An HP frequency counter (Model 5302A) was used to measure frequency. AT-cut quartz crystals with a 10 MHz fundamental resonance frequency were used. Gold films of 200 nm thickness were deposited onto both sides of the quartz disks in a "keyhole" shape. The quartz disks were primed with 15 nm of chromium prior to gold deposition. The gold film has an excitation

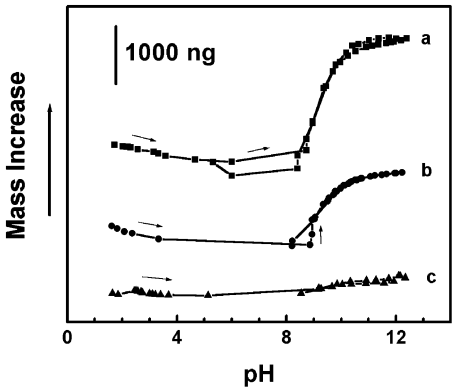

Figure 1. Mass change vs pH curves in 0.5 M KCl for MUA−Au_{2-nm} films with different thicknesses (number of equivalent layers): 302 (a), 193 (b), and 68 (c).

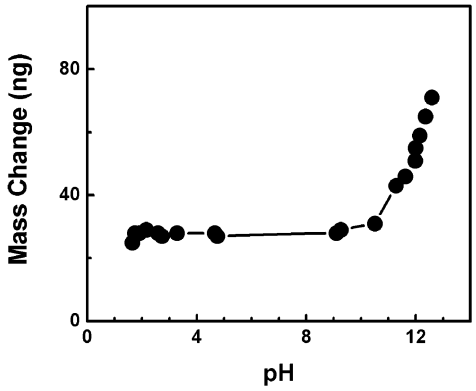

Figure 2. Mass change vs pH curves in 0.5 M KCl for a MUA−Au_{5-nm} film (five layers).

piezoelectrode area of 0.2 cm^2 and an electrochemical active electrode area of 0.25 cm^2. The resonance frequency was determined prior to and after the film deposition, which provides a measure of the film thickness.[19c]

Results and Discussion

This section is divided into two parts. The first part presents data from probing pH-tuned interfacial responses at the MUA-linked gold nanoparticle films. The second part describes data from probing the interfacial mass fluxes of the nanostructure upon binding of redox metals. On the basis of these studies, we also discuss the charge−mass correlation and implications of the findings.

pH-Tuned Responses. *Protonation/Deprotonation Characteristic.* The protonation and deprotonation property is best characterized by interfacial titration curves which can be determined by EQCN-detected mass change as a function of pH at a film-coated piezoelectrode. Figure 1 shows a representative set of titration curves for MUA−Au_{2-nm} films of three different thicknesses in terms of equivalent number of nanoparticle layers.[31] The common feature of these curves is the mass rise at pH ∼8 followed by a gradual leveling off toward a plateau at pH ∼11. At pH <8, the mass change is insignificant. The overall mass change is reversible, as reflected by the overlap of both forward and reversing data points between pH 8 and 12. The mass change is attributed to fluxes of protons, cations (K^+), and solvent from the electrolyte solution into the film as a result of the protonation−deprotonation of the carboxylic acid groups in the ligand framework.

The magnitude of the mass change is dependent on the film thickness. The mass changes determined from the above data are 1.1, 5.2, and 9.5 $\mu g/cm^2$ for the films of 68, 193, and 302 layers, respectively. The middle point between the onset of the mass rise to the onset of the plateau provides a measure of pK_a value for the carboxylic acid groups in the film. Interestingly, the data for these films of different thickness yield almost the same pK_a, i.e., ∼9.5. This observation indicates that their accessibilities to ions and solvent molecules are comparable in this thickness range. We note however that, for a very thick film (>461 equivalent layers), we observed a unusual loop between the mass rise and the mass return curves in a broad pH range (pH 2.8−11.5). Outside this range, the mass changes were switchable in a reversible way. The exact origin of this switching loop is still under further investigation. A possible contribution is from resonant frequency shifts due to the energy dissipation associated with inelastic film deformation of swollen films.

TABLE 1: Mass Changes for a MUA−Au_{5-nm} Film (Six Layers) Emersed from Several Different pHs[a]

pH	Δm ($\mu g/cm^2$)
2.39	0.54 ± 0.25
5.73	1.17 ± 0.24
11.76	1.97 ± 0.27

[a] The film was dried after emersion.

The size of the nanoparticle cores also plays an important role in the pH-tuned characteristic. Figure 2 shows a representative set of titration curve for a MUA−Au_{5-nm} film of five equivalent layers. It is evident that the qualitative trend of the mass change is similar to that observed for the MUA−Au_{2-nm} film. The total mass change was 0.25 $\mu g/cm^2$. A close comparison between the data from the two different core sizes reveals a major difference. The onset of the mass rise is shifted to a higher pH by about 1 pH unit (∼9.0). Although it is not apparent to identify the mass plateau, we estimated the pK_a to be 11.5−12.0, which was higher than that for the MUA−Au_{2-nm} film by about two pH units. We believe that this difference reflects the difference of density (or concentration) of the $-CO_2H$ groups in the film. Different core sizes may lead to a difference in terms of the number of ligand molecules in a unit volume of the nanostructure. Our recent studies[31] revealed that the percentage of $-CO_2H$ groups within a MUA−Au_{2-nm} film is much higher than that in a MUA−Au_{5-nm} film, as reflected by their differences in solubility properties in different solvents and diagnostic infrared[19b] and NMR spectroscopic bands.[31,32]

To further assess the solvent contribution to the overall mass change, we also performed an ex situ measurement of the mass change of the film by emersion of the film from solutions of different pHs followed by air-drying. A representative set of data for MUA−$Au_{5\ nm}$ film (six equivalent layers) emersed from three different pHs is shown in Table 1. The film was coated with a few monolayers of polystyrene to render the surface hydrophobic.[33] This treatment does not affect the electrolyte accessibility because the polymer forms a loose layer as observed by atomic force microscopy (AFM). The immersion time was 5 min at each pH. The results clearly show that the mass increases with pH, which is qualitatively consistent with the EQCN data described earlier. Quantitatively, the total mass increase from pH 2 to 12, ∼0.6 $\mu g/cm^2$ (one side) is about 2 times larger than the mass change detected by EQCN for the same film thickness. This result may suggest that the water molecules entered into the deprotonated film are difficult to be completely removed in the experimental time scale (10 min). A more in-depth study of the solvent effect and the possibility of water crystallization in the nanostructure is under way.

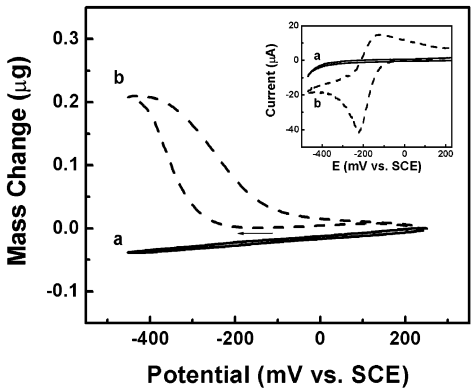

Figure 3. Mass change curves for MUA−Au_{2-nm} film (235 layers) in 1.0 mM $Ru(NH_3)_6^{3+}$/0.5 M KCl solutions at pH 2.7 (a) and 10.7 (b). Scan rate: 50 mV/s. Inset: Corresponding cyclic voltammetric curves.

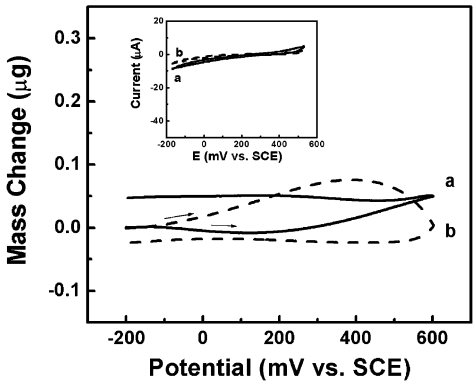

Figure 4. Mass change curves for MUA−Au_{2-nm} film (235 layers) in 1.0 mM $Fe(CN)_6^{3-}$/0.5 M KCl solutions at pH 2.7 (a) and 10.7 (b). Scan rate: 50 mV/s. Inset: Corresponding cyclic voltammetric curves.

Ion Gating. On the basis of the above analysis, we next examined the mass change characteristic for the pH-tuned redox reaction. We recently reported electrochemical data showing the ion gating property of the film toward redox ions.[19b] The EQCN experiment here is to assess the associated mass flow through the network regulated by the nanostructured ligand framework binding specificity. Ionic redox probes of two different signs, i.e., $[Fe(CN)_6]^{3-/4-}$ and $[Ru(NH_3)_6]^{3+/2+}$, were examined.

Figure 3 shows a representative set of mass change curves for a piezoelectrode coated with a MUA−Au_{2-nm} film in the presence of $[Ru(NH_3)]_6^{3+}$ at two different pHs. The corresponding voltammetric current curves (inset)[19b] are included for comparison, which shows ion gating behavior as evidenced by the redox waves (−320 mV) at pH 11 and the featureless background at pH 2. At pH 2, the mass change is insignificant, which is in excellent agreement with the lack of redox current in the voltammetric curve. In contrast, a distinctive mass change profile is detected at pH 11. The mass increases in the negative potential sweep and returns in the positive potential sweep. Qualitatively, this observation is suggestive of incorporation of electrolyte species during the reduction of $Ru(NH_3)_6^{3+}$ which is electrostatically associated with the negatively fixed charges ($-CO_2^-$ group) in the film. For reason of electroneutrality, the reduction process requires the supply of positive charges to compensate the fixed negative $-CO_2^-$ groups. Therefore, it is likely that K^+ cations flux into the film during the reduction and flux out upon reoxidation.

Such a redox reaction induced ionic flux is interesting because it can be manipulated or triggered not only chemically (by pH) but also electrochemically (by applied potential). At pH 11, the detected mass change for the reduction (1.2 μg/cm^2) is quite large in comparison with the relatively small reduction charge (489 μC/cm^2) which corresponds to 0.20 μg/cm^2 of K^+ ions. Since the detected mass change is much larger than the expectation simply based on the take-in of K^+ cations, the flux of solvent molecules must have been involved. We also note that there is a small mass change at pH 2. The mass increases linearly and reversibly from negative to positive potentials. This mass change (0.19 μg/cm^2) is probably indicative of a potential-dependent double layer charging at the electrode|film|electrolyte interfaces, the details of which are under investigation.

The mass change profile is also dependent on the charge of the redox probe. Figure 4 shows a representative set of mass curves for a piezoelectrode coated with a MUA−Au_{2-nm} film in the presence of $Fe(CN)]_6^{3-}$ at two different pHs. The corresponding voltammetric current curves (inset)[19b] are included for comparison, which displays a silent voltammetric background feature at both high and low pHs. In sharp contrast to the mass change profile observed in the presence of the cationic redox probe (Figure 4), the mass changes detected here are much smaller at both low and high pHs. This observation demonstrates that the incorporation of the negatively charged redox ion is largely blocked at both pHs due to the repulsive effect between the probe and the negative charges residing at the rim of the nanostructured channels. We note, however, that there are subtle mass changes at both pHs. The small mass increase from negative to positive potential (0.28 μg/cm^2) at pH 3, while not completely reversible, is consistent with the data in the presence of $Ru(NH_3)_6^{3+}$, which is attributed to possible double layer charging effect. The small mass wave at $\sim$ +400 mV (0.38 μg/cm^2) at pH 11 is likely due to leakage at defects of the deprotonated film. This effect is likely responsible for the lack of reversibility of the mass curves. We have also studied other redox probes such as neutral and cationic ferrocenes (e.g., trimethylaminomethylferrocenyl), and catechol, which provided additional confirmation of the gating properties.

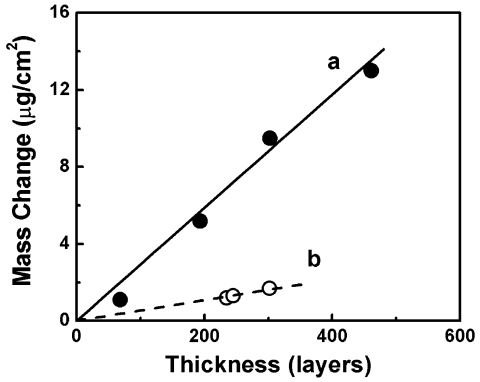

Figure 5. Total mass change vs film thickness from pH 2 to 11 in 0.5 M KCl (a) and 1.0 mM $Ru(NH_3)_6^{3+}$/0.5 M KCl (b).

Implications. The above mass change data demonstrate that pH tuning at the nanostructured films can lead to a reversible ionic flux across the film. The flux is dependent on a combination of factors: (1) the degree of protonation−deprotonation at the interparticle linkages, (2) the sizes of the particle core, (3) the thickness of the film, and (4) the charges and sizes of the redox probe. The understanding of these factors has important implications to the manipulation of the ion gating properties at both nanocrystal and molecular levels.

One of the most remarkable observations is the large magnitude of mass changes for the cationic flux in the presence and in the absence of redox probes. Figure 5 plots the total mass change as a function of film thickness. In the absence of

redox probe, it displays basically a linear relationship. A comparison of the experimentally determined mass change with a theoretically estimated mass change provides additional insight. The percentage of the total mass change in the total mass of the film between the two pHs is about 4−8%. The lower end of this percentage (for a thin film of ∼68 layers) is close to the theoretical value estimated for a fully K^+-loaded film (4.7 wt %). The fact that the values obtained for thicker films are larger than the theoretical value suggests that there must be a significant involvement of solvent molecules in the interfacial mass flux. This finding is intriguing because it implies that the equilibrium accessibility by cations and solvent molecules from the electrolyte does not seem to be affected by the film thickness when the film is relatively thin. For very thick MUA−Au_{2-nm} film (∼500 layers), the kinetic effect may play a role in affecting the accessibility. Upon further investigation, this phenomenon may be utilized for designing a pH-switchable film for ion storage and delivery.

The striking mass change has in fact shined a further light on morphological changes observed earlier using AFM.[34] In agreement with the EQCN detection of a large amount of cations and solvent molecules in the film, the AFM data for a MUA−linked Au_{5-nm} film selectively assembled on patterned MUA squares revealed a topographical height change of 13.6 nm between pH 2 and 12. The magnitude of the height change is much larger than the expectation simply based on the cationic incorporation into the interparticle regions, which is to our knowledge not reported for other nanoparticle assemblies. In addition to tip−sample electrostatic interactions, it is likely that the deprotonated film "swells" due to flux of ions and solvent across the film. This implies a highly nanoporous membrane whereby solvent and ions are reversibly loaded and released by changing pH.

In addition to pH tuning, the viability of ion flux regulation by the incorporated redox ions is interesting as indicated by a further comparison of the total mass changes detected in the presence and in the absence of $[Ru(NH_3)]_6^{3+}$ (Figure 5, dashed line). Both mass changes exhibit approximately a linear relationship. On the basis of the ratio of the slopes, there is a 5.5-fold decrease for the mass flux detected from the presence of the redox ions. This difference suggests the incorporation of $[Ru(NH_3)]_6^{3+}$ into the film. By correlation with the film thickness, the mass change for the incorporated amount of redox ions translates to ∼6% of the total mass of the film. The fact that this loading level of redox probe can regulate the incorporation and release of cations is intriguing for potential applications in controlled drug release. There is unfortunately a propensity for leaching of the incorporated $[Ru(NH_3)]_6^{3+}$ due to a weak electrostatic interaction. In the next part, we will describe the use of nanostructures loaded with redox metals for testing the viability of controlled incorporation and release.

For the possible ion-exchange processes in the presence of $Ru(NH_3)_6^{3+}$ and K^+ to replace hydrogen ions, we consider the following electroneutrality conditions:

$$2(-COOH) + 2K^+ = 2(-COO^-\cdot K^+) + 2H^+ \quad \text{(in KCl solution)} \quad (1a)$$

$$3(-COOH) + Ru(NH_3)_6^{3+} = Ru(NH_3)_6^{3+}(-COO^-)_3 + 3H^+ \text{(in Ru(III) solution)} \quad (1b)$$

Since the experimentally observed ratio is much larger (ca. 5.5) than the corresponding reaction molar mass changes, there is likely substantial solvent involvement, especially in the KCl solution. The multivalent Ru(III) complex attracts electrostatically carboxylate groups to maintain a tighter structure, thus preventing solvent ingress. In contrast, K^+ ions provide a weak binding and thus more water molecules can be accommodated in the interparticle space.

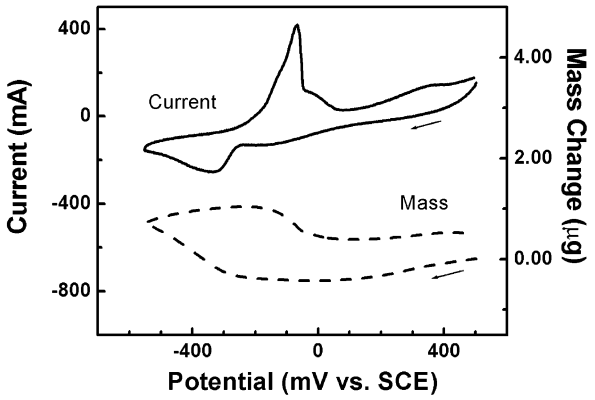

Figure 6. EQCN curves for MUA−Au_{2-nm} film (245 layers) in 5.0 mM $Cu(NO_3)_2$/0.5 M KCl solution. Scan rate: 50 mV/s.

Redox-Regulated Responses. *Loading of Redox Metal.* To manipulate the nanostructured electroactivity, the viability of loading of redox metal ions in the nanostructure and the interfacial mass fluxes associated with the redox activity were examined. While we studied a series of metal ions, we focus on the results from the study of copper ion. We note that Cu^{2+}−carboxylate complexation chemistry has been explored early for chemical sensors at self-assembled monolayers[5,6] and recently for linking nanoparticles into assembly[17] and colorimetric detection of metal ions.[21] Figure 6 shows a representative set of EQCN curves for MUA−Au_{2-nm} thin film (245 layers) coated piezoelectrode in 5.0 mM Cu^{2+}/0.5 M KCl solution (pH of the electrolyte ∼4.5). The current curve displays redox waves corresponding to Cu^{2+}/Cu^0 redox reaction which are partially characteristic of bulk deposition of Cu in the film, and partially due to the low electronic conductivity of the film (∼10^{-6} S/cm).[23] While the film blocks surface sites for UPD reactivity,[20] it does admit Cu^{2+} and thus exhibits bulk deposition redox electroactivity. The mass curve shows a mass increase (7.3 μg/cm^2) corresponding to the reduction and a mass decrease (3.3 μg/cm^2) corresponding to the oxidation. There is a net increase of mass (4.0 μg/cm^2) after one cycle.

To confirm the incorporation of Cu^{2+} into the film, we examined the transient response of the MUA−Au_{2-nm} film (193 layers) upon injection of Cu^{2+} into the solution at open circuit potential (0.15 V). The gradual increase of the mass (Figure 7) indicates a spontaneous incorporation of copper ions into the nanostructured ligand framework. Since the access of solution anions to the film matrix is strongly inhibited by the presence of negative fixed charges of the linker, the copper ion ingress has to be compensated by the egress of cations ($M^+ = H^+$ or K^+) from the film (f), as required by the charge balance. In the case of $M^+ = H^+$, we have

$$Cu^{2+}(aq) + 2H^+(f) = Cu^{2+}(f) + 2H^+(aq) \quad (2a)$$

The mass balance for this reaction is positive ($\Delta M = M_{Cu} - 2M_H = 61.5$ g/mol) which is consistent with the experimentally observed mass change. If the film is treated with base, i.e., $M^+ = K^+$, a simple ion-exchange reaction

$$Cu^{2+}(aq) + 2K^+(f) = Cu^{2+}(f) + 2K^+(aq) \quad (2b)$$

would be inconsistent with the experimentally observed mass

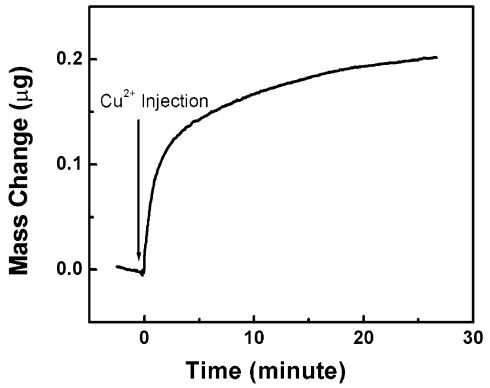

Figure 7. Apparent mass change transient curve for MUA−Au_{2-nm} film (193 layers) in 0.5 M KCl upon injection of $Cu(NO_3)_2$ (final concentration: 5.0 mM).

change since the mass balance for this reaction is negative ($\Delta M = M_{Cu} - 2M_K = -14.6$ g/mol). For the latter case, we are carrying out a more detailed analysis (e.g., X-ray photoelectron spectroscopy) of the incorporated species to assess whether copper is in fact complexed by chloride to form weak $CuCl^+$ complexes (stability constant: $K_1 = 6.3 \times 10^2$ M^{-1}),[35] under which the mass change ($\Delta M_2 = M_{CuCl} - M_K = 59.9$ g/mol) would be positive.

The detected mass change, 1.0 μg/cm^2 in ~25 min, translates to 1.3% of the total mass. This value is smaller than the theoretically estimated value for a fully Cu^{2+}-loaded film of the same thickness (3.8 wt %) (or a $CuCl^+$-loaded film of the same thickness (11.8 wt %)). This level of Cu^{II} loading is believed to reflect a combination of factors such as the low pH of the electrolyte, the lack of sufficient equilibrium time, and the lack of a full accessibility of the film because of relatively rigid nanostructure.

Figure 8 shows a representative set of EQCN curves for the MUA−Au_{2-nm} film (245 layers) in a 0.5 M KCl solution after being taken out of the Cu(II) solution and thoroughly rinsed. The EQCN curves (A) for the film before exposure to the Cu(II) solution are included for comparison. The curve for the before-exposure film (A) is basically featureless. In contrast, both current and mass responses are detected for the after-exposure film (B). In the current curve, the peak separation (ΔE_p ~ 475 mV) is larger than that for the film in the presence of Cu(II) (ΔE_p ~ 300 mV) due to the low conductivity and thickness effects of the MUA−Au_{2-nm} film. The Cu-loaded film is chemically reversible as evidenced by the fact that the integrated cathodic charge density ($Q_c = 678$ μC/cm^2) is comparable with the anodic charge ($Q_a = 605$ μC/cm^2). An estimate from the average charge yields 3.6×10^{-9} mol/cm^2 Cu^{2+}. The conversion of the charge to electrolyte cations yields 0.14 μg/cm^2 in terms of its mass equivalency to K^+ ion.

In the mass curve, a reversible change in mass release and intake in the redox reaction of Cu(II) + 2e = Cu is evident. The detected mass change is believed to be due to the flux of cations from the electrolyte into the film to compensate the negative fixed charges left as a result of the reduction of copper ions. The mass increase, ~3 μg/cm^2, corresponds to an equivalency of 7.7×10^{-8} mol/cm^2 K^+. This quantity is about 1 order of magnitude larger than the mass change estimated from the redox charge (0.14 μg/cm^2), indicating there is a large flux of solvent molecules accompanying the ionic flux. The above assessment is schematically illustrated in Scheme 2. This observation is remarkable because the ionic and solvent flux could be manipulated by redox reaction in the thin film.

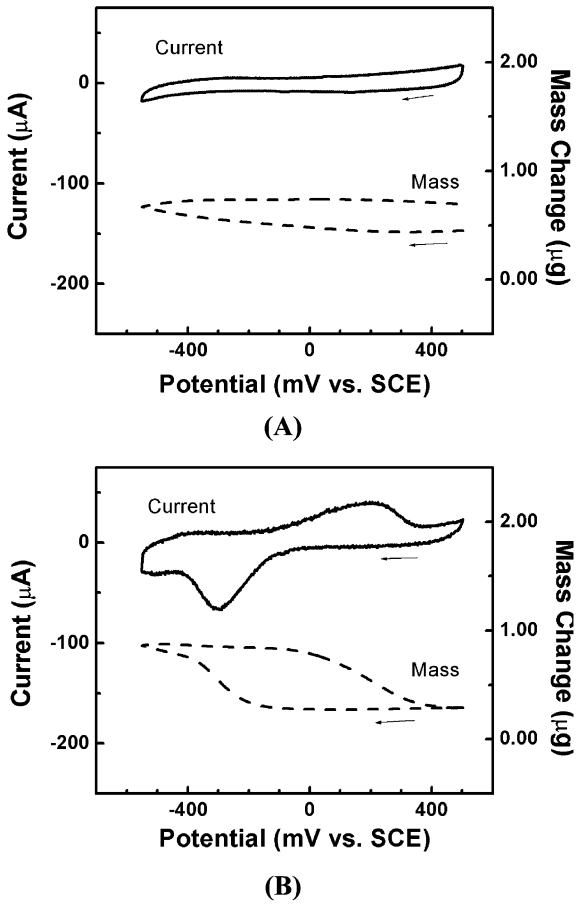

Figure 8. EQCN curves for MUA−Au_{2-nm} film (245 layers) in 0.5 M KCl before (A) and after (B) being exposed to Cu^{2+} solution (5 mM $Cu(NO_3)_2$/0.5 M KCl, exposure time ~10 min). The film was thoroughly rinsed with water after exposure. Scan rate: 50 mV/s.

SCHEME 2: Schematic Illustration of Cation (M^+) and Solvent (S) Fluxes at the Electrode|Film|Electrolyte Interface upon Electrochemical Oxidation and Reduction of Incorporated Cu(II)

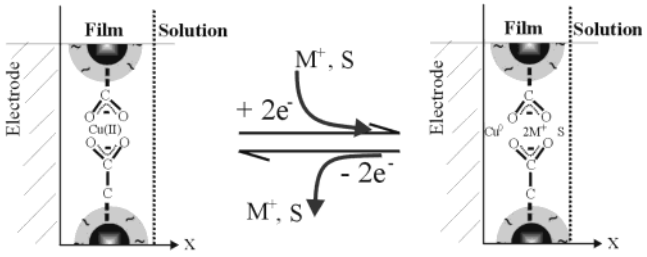

Responses to Electrolytic Cations. The above results clearly demonstrated that the electrolyte ions incorporated into the Cu^{2+}-loaded MUA−Au_{2-nm} film could be released upon reversing the potential sweeping direction. To understand the chemical basis of this interfacial phenomenon, we next investigated mass fluxes of the film in the presence of a series of different electrolyte cations.

Figure 9 shows a typical set of EQCN data at the Cu-loaded film for a series of cations, including Li^+, K^+, Rb^+, and Cs^+ (A), and NH_4^+ and $N(CH_3)_4^+$ (B). Here we used a relatively thick film of MUA−Au_{2-nm} (389 layers). Qualitatively, all these ion species follow the same trend in mass change profile. Quantitatively, the magnitude of the mass change can be correlated to the mass of the ionic species. It is evident that the magnitude of the mass response increases in the order of Li^+

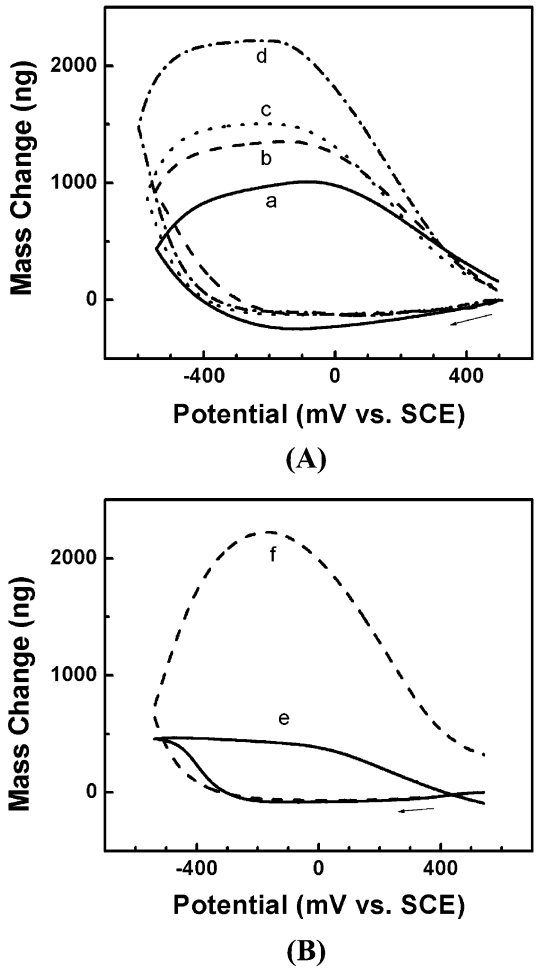

Figure 9. EQCN curves for Cu^{II}-loaded MUA−Au_{2-nm} film (389 layers) in LiCl (a), KCl (b), RbCl (c), CsCl (d), NH_4Cl (e), and $N(CH_3)_4$-Cl (f) electrolytes (all 0.1 M). Scan rate: 50 mV/s.

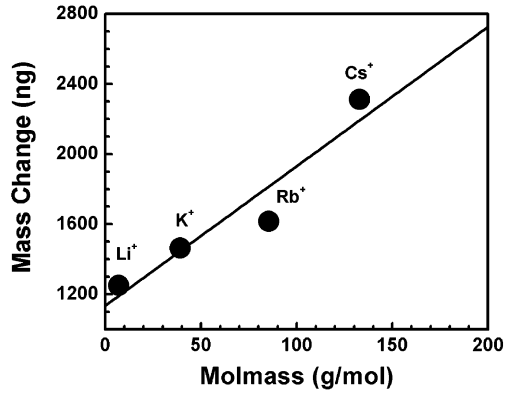

Figure 10. Plot of total mass change vs molar mass of the electrolyte cation for a Cu^{II}-loaded MUA−Au_{2-nm} film (389 layers).

$< K^+ < Rb^+ < Cs^+$. For ammonium species, the magnitude of the mass response increases in the order of $NH_4^+ < N(CH_3)_4^+$ (B).

In Figure 10, the mass change data are plotted against the molar mass for a series of metal ions (Li^+, K^+, Rb^+, and Cs^+). The plot displays a good linear relationship between the detected mass change and the atomic weight of the cation. A relatively large intercept (1136 ng or 5.68 $\mu g/cm^2$) is, however, found, which we believe reflects the influx of solvent molecules. While this mass flux will be further correlated with solvent intake in the next subsection, we note that water intake may not increase proportionally with the film thickness. Experiments indicate that there might be a certain threshold in terms of the film thickness, after which films begin to swell. We are currently conducting a comparative study of EQCN and AFM measurements to determine water intake from the intercept of mass change vs thickness and vs different electrolyte cations. The result has demonstrated that the mass change is directly related to the nature of the metal ions, which could form the basis of a novel class of nanomaterials for detection of metal ions and controlled release applications.

We have also studied the response characteristics of the film to other metal ions (e.g., Hg^{2+}, Cd^{2+}, etc). The results provided additional insights into the ionic flux and binding properties, details of which will be reported in the future, along with studies of its application in controlled release of cationic drugs.

Charge−Mass Correlation. We consider now the total mass change observed during the reduction process of the loaded Cu^{2+} in different electrolyte solutions. The reduction of Cu^{2+} in the film takes place during the cathodic potential scan, from $E = -100$ mV to the reversal potential at $E = -550$ mV, and after the reversal, during the initial portion of the anodic scan until the potential $E = -100$ mV is attained, i.e., until copper begins to oxidize. The total mass change observed is attributed to the ion-exchange processes at the film|solution interface and possible ingress/egress of solvent molecules:

$$\Delta m = \sum_j \frac{q_j M_j}{n_j F} + \Delta m_{aq} \tag{3}$$

where Δm_{aq} is the mass change due to solvent intake, q_j is the total charge carried by species j, n is the number of elementary charges on ions, and M is their molar mass. The charge q_j is considered positive for cations entering the film and negative for cations leaving the film, and opposite relations hold for anions. The ion-exchange processes reflected in eq 3 are coordinated by the film electroneutrality condition:

$$\sum_j q_j + Q_c = 0 \tag{4}$$

where

$$Q_c = \int \frac{i(E)}{\upsilon} dE - C_{int} \upsilon \Delta t \tag{5}$$

is the charge consumed for copper(II) reduction ($Q_c < 0$), $i(E)$ is the total current, C_{int} is the integral capacitance representing the double-layer capacitance and low-frequency component of film capacitance, and $\upsilon = \partial E/\partial t$. We assume that there is no significant exchange of Cu(I) and Cu(II) species with the medium during the time scale of experiments: $\Delta m_{Cu(II)} \approx 0$. This assumption is justified by the copper coordination at the carboxylate groups. A small loss of copper due to the establishment of Donnan equilibrium with new electrolyte solution is negligible as evidenced by good reproducibility of mass-potential characteristics in consecutive potential cycles. The exchange of electrolyte anions is also negligible due to strong repulsive forces between anions and negatively charged functional groups of the linker. Also, the chemical potential of chloride ions is the same for all solutions used in these measurements. Hence, $\Delta m_{Cl^-} \approx 0$ and $q_{Cl^-} \approx 0$. The electroneutrality condition must be satisfied solely by the movement of electrolyte cations M^+: $q_{Me^+} = -Q_c$. Equation 3 is therefore simplified to

$$\Delta m = \frac{-Q_c M_{M^+}}{F} + \Delta m_{aq} \quad (6)$$

where Q_c is constant for the entire series of electrolytes. By plotting Δm vs M_{M^+} (molar mass of the cation), the contribution of solvent uptake or release to the observed mass change can then be evaluated from the intercept Δm_{aq}. From the experimental plot for Li^+, K^+, Rb^+, and Cs^+ and its linearity, the slope $\partial\Delta m/\partial M = 7.6 \times 10^{-9}$ mol and intercept $\Delta m_{aq} = 1150$ ng, which corresponds to the mass density $\Delta m_{aq}^* = 5858$ ng/cm^2 (i.e., mass per geometric surface area). We can further derive the mass of solvent per monolayer (ML) of Au nanoparticles:

$$\Delta m_1 = \Delta m^*/n_{ML} = 5858.4/389 = 15.0 \text{ ng/ML}$$

where the number of equivalent monolayers $n_{ML} = 389$. The mass of solvent per unit surface area of Au nanoparticles is then

$$\Delta m_2 = \Delta m_1/S_{\text{Au mono}} = 15.0/0.515 = 29.1 \text{ ng/cm}^2$$

where $S_{\text{Au mono}} = 0.515$ cm^2/ML is the deconvoluted surface area of a monolayer of spherical nanoparticles. It follows from model considerations that one water molecule per one Au nanoparticle leads to the mass change in one monolayer of such particles:

$$\Delta m_3 = \frac{M_{H_2O}}{N_0} n_{mono} = \frac{18}{6.022 \times 10^{23}} 4.1 \times 10^{12} = 0.123 \text{ ng/ML} \quad (7)$$

Since the experimental mass change due to the solvent uptake is given by Δm_1, we can calculate the number of water molecules per Au particle:

$$n(H_2O) = \Delta m_1/\Delta m_3 = 15.0/0.123 = 122$$

This is indeed a significant amount of solvent accompanying the ion flux in the redox reaction of the incorporated Cu^{II} species. For a fully MUA-capped Au_{2-nm} particle model, there are about 70 carboxylate groups. This number translates to 35 sites with Cu^{2+}. The calculated results thus imply that each site has two to four water molecules. As noted in the previous section, the particles are only partially capped with MUA, i.e., with about 45% of the surface sites functionalized with carboxylates.[31] This corresponds to 5−10 water molecules per carboxylate ligand, an assessment consistent with our previous AFM observation of the swelling property for the nanostructured thin film.[34]

Conclusion

In conclusion, we have demonstrated that the thin films assembled from decanethiolate-capped gold nanocrystals and carboxylic acid functionalized thiol linkers serve as an intriguing model system for probing interfacial physical and chemical phenomena. The nanostructured three-dimensional ligand framework has a large surface area-to-volume ratio and binding specificity for incorporating metal and redox ions. The EQCN results reveal four distinctive mass response characteristics upon pH tuning or metal ion binding. First, the protonation−deprotonation characteristic of the carboxylic acid groups in the nanostructured framework is dependent on particle core size and film thickness. For relatively thin films, a pK_a value of ~10 was determined. The difference in relative density and accessibility of carboxylic acid groups in the nanostructured films are believed to play important roles in the observed size and thickness dependencies. Second, the pH-tunable cationic redox reaction across the electrode|film|electrolyte interface is accompanied by a large cationic electrolyte mass flux. In the presence of redox reaction, a large increase of mass was detected at pH 11 for the reduction of cationic probe ($[Ru(NH_3)_6]^{3+/2+}$). In contrast, such a mass change was not detected for the reduction of anionic probe ($[Fe(CN)_6]^{3-/4-}$). The reversible mass change reflects the intake and release of cations from the electrolyte that electrostatically balances the fixed negative charge. Third, the spontaneous complexation to copper ions by the nanostructured carboxylate framework is reflected by mass increase of the film. We believe that such metal binding capability can be expanded to many other metal ions. Fourth, the redox reaction of copper loaded in the nanostructured film is accompanied by fluxes of electrolyte cations across the electrode|film|electrolyte interface which compensate electrostatically the fixed negative charges. On the basis of the mass change detected in the presence of a series of electrolyte cations, a linear relationship was determined between the mass increase and the molar mass of the cation, and a concurrent flux of solvent molecules is also revealed. These findings are important for further delineation of the design parameters of nanostructured materials for controlled release and environmental monitoring of metals. In view of the simplicity and low detection limit of the EQCN device, and the high surface area-to-volume ratio, tunable ligand framework, and conductivity of the nanostructured materials, the nanoparticle-tailored EQCN detection, upon further investigation in systems with mixed analytes, is potentially amenable for developing a simple, rapid, sensitive, and selective monitoring device for heavy metals. More experiments are clearly needed to assess the analytical figures of merit and stability issues for different heavy metals from environmental samples.

Acknowledgment. Financial support of this work from the Petroleum Research Fund administered by the American Chemical Society, ACS-SRF, and the 3M Corporation is gratefully acknowledged.

References and Notes

(1) Shipway, A. N.; Katz, E.; Willner, I. *Chem. Phys. Chem.* **2000**, *1*, 18.
(2) Niemeyer, C. M. *Angew. Chem., Int. Ed.* **2001**, *40*, 4128.
(3) Gutierrez, E.; Miller, T. C.; Gonzalez-Redondo, J. R.; Holcombe, J. A. *Environ. Sci. Technol.* **1999**, *33*, 1664.
(4) (a) Miller, T. C.; Holcombe, J. A. *Anal. Chem.* **1999**, *71*, 2667. (b) Hepel, M.; Dentrone, L. *Electroanalysis* **1996**, *8*, 996.
(5) Thomas, R. C.; Yang, H. C.; DiRubio, C. R.; Ricco, A. J.; Crooks, R. M. *Langmuir* **1996**, *12*, 2239.
(6) Steinberg, S.; Tor, Y.; Sabatani, E.; Rubinstein, I. *J. Am. Chem. Soc.* **1991**, *113*, 5176.
(7) Templeton, A. C.; Wuelfing, W. P.; Murray, R. W. *Acc. Chem. Res.* **2000**, *33*, 27 and references therein.
(8) Whetten, R. L.; Shafigullin, M. N.; Khoury, J. T.; Schaaff, T. G.; Vezmar, I.; Alvarez, M. M.; Wilkinson, A. *Acc. Chem. Res.* **1999**, *32*, 397.
(9) Link, S.; El-Sayed, M. A. *Int. Rev. Phys. Chem.* **2000**, *19*, 409.
(10) Brust, M.; Walker, M.; Bethell, D.; Schiffrin, D. J.; Whyman, R. *J. Chem. Soc., Chem. Commun.* **1994**, 801.
(11) (a) Templeton, A. C.; Hostetler, M. J.; Kraft, C. T.; Murray, R. W. *J. Am. Chem. Soc.* **1998**, *120*, 1906. (b) Wuelfing, W. P.; Templeton, A. C.; Hicks, J. F.; Murray, R. W. *Anal. Chem.* **1999**, *71*, 4069. (c) Chen, S. W.; Murray, R. W. *J. Phys. Chem. B* **1999**, *103*, 9996. (d) Templeton, A. C.; Cliffel, D. E.; Murray, R. W. *J. Am. Chem. Soc.* **1999**, *121*, 7081. (e) Green, S. J.; Stokes, J. J.; Hostetler, M. J.; Pietron, J.; Murray, R. W. *J. Phys. Chem. B* **1997**, *101*, 2663. (f) Hostetler, M. J.; Wingate, J. E.; Zhong, C. J.; Harris, J. E.; Vachet, R. W.; Clark, M. R.; Londono, J. D.; Green, S. J.; Stokes, J. J.; Wignall, G. D.; Glish, G. L.; Porter, M. D.; Evans, N. D.; Murray, R. W. *Langmuir* **1998**, *14*, 17. (g) Hostetler, M. J.; Templeton, A. C.; Murray, R. W. *Langmuir* **1999**, *15*, 3782.

(12) (a) Brust, M.; Bethell, D.; Kiely, C. J.; Schiffrin, D. J. *Langmuir* **1998**, *14*, 5425. (b) Brust, M.; Bethell, D.; Schiffrin, D. J.; Kiely, C. J. *Adv. Mater.* **1995**, *7*, 795. (c) Bethell, D.; Brust, M.; Schiffrin, D. J.; Kiely, C. *J. Electroanal. Chem.* **1996**, *409*, 137. (d) Brust, M.; Kiely, C. J.; Bethell, D.; Schiffrin, D. J. *J. Am. Chem. Soc.* **1998**, *120*, 12367. (e) Baum, T.; Bethell, D.; Brust, M.; Schiffrin, D. J. *Langmuir* **1999**, *15*, 866. (f) Horswell, S. L.; O'Neil, I. A.; Schiffrin, D. J. *J. Phys. Chem. B* **2001**, *105*, 941. (g) Gittins, D. I.; Bethell, D.; Schiffrin D. J.; Nichols, R. J. *Nature* **2000**, *408*, 67.

(13) (a) Hostetler, M. J.; Green, S. J.; Stokes, J. J.; Murray, R. W. *J. Am. Chem. Soc.* **1996**, *118*, 4212. (b) Ingram, R. S.; Hostetler, M. J.; Murray, R. W. *J. Am. Chem. Soc.* **1997**, *119*, 9175. (c) Templeton, A. C.; Hostetler, M. J.; Warmoth, E. K.; Chen, S. W.; Hartshorn, C. M.; Krishnamurthy, V. M.; Forbes, M. D. E.; Murray, R. W. *J. Am. Chem. Soc.* **1998**, *120*, 4845.

(14) (a) Musick, M. D.; Pena, D. J.; Botsko, S. L.; McEvoy, T. M.; Richardson, J. N.; Natan, M. J. *Langmuir* **1999**, *15*, 844. (b) Keating, C. D.; Musick, M. D.; Lyon, L. A.; Brown, K. R.; Baker, B. E.; Pena, D. J.; Feldheim, D. L.; Mallouk, T. E.; Natan, M. J. *ACS Symp. Ser.* **1997**, *679*, 7.

(15) (a) Mirkin, C. A.; Letsinger, R. L.; Mucic, R. C.; Storhoff, J. J. *Nature* **1996**, *382*, 607. (b) Elghanian, R.; Storhoff, J. J.; Mucic, R. C.; Letsinger, R. L.; Mirkin, C. A. *Science* **1997**, *277*, 1078.

(16) Zhong, C. J.; Maye, M. M. *Adv. Mater.* **2001**, *13*, 1507.

(17) (a) Zamborini, F. P.; Hicks, J. F.; Murray, R. W. *J. Am. Chem. Soc.* **2000**, *122*, 4514. (b) Templeton, A. C.; Zamborini, F. P.; Wuelfing, W. P.; Murray, R. W. *Langmuir* **2000**, *16*, 6682.

(18) (a) Lahav, M.; Gabai, R.; Shipway, A. N.; Willner, I. *Chem. Commun.* **1999**, 1937. (b) Lahav, M.; Shipway, A. N.; Willner, I. *J. Chem. Soc., Perkin Trans.* **1999**, *2*, 1925. (c) Liu, J.; Alvarez, J.; Kaifer A. E. *Adv. Mater.* **2000**, *12*, 1381. (d) Liu, J.; Mendoza, S.; Roman, E.; Lynn, M. J.; Xu, R. L.; Kaifer, A. E. *J. Am. Chem. Soc.* **1999**, *121*, 4304. (e) Mayya, K. S.; Patil, V.; Sastry, M. *Langmuir* **1997**, *13*, 3944.

(19) (a) Leibowitz, F. L.; Zheng, W. X.; Maye, M. M.; Zhong, C. J. *Anal. Chem.* **1999**, *71*, 5076. (b) Zheng, W. X.; Maye, M. M.; Leibowitz, F. L.; Zhong, C. J. *Anal. Chem.* **2000**, *72*, 2190. (c) Han, L.; Maye, M. M.; Leibowitz, F. L.; Ly, N. K.; Zhong, C. J. *J. Mater. Chem.* **2001**, *11*, 1259.

(20) Israel, L. B.; Kariuki, N. N.; Han, L.; Maye, M. M.; Luo, J.; Zhong, C. J. *J. Electroanal. Chem.* **2001**, *517*, 69.

(21) Kim, Y. J.; Johnson, R. C.; Hupp, J. T. *Nano Lett.* **2001**, *1*, 165.

(22) Boal, A. K.; Rotello, V. M. *Langmuir* **2000**, *16*, 9527.

(23) Hao, E.; Lian, T. *Chem. Mater.* **2000**, *12*, 3392.

(24) (a) Bryant, M. A.; Crooks, R. M. *Langmuir* **1993**, *9*, 385. (b) Wang, J.; Frostman, L. M.; Ward, M. D. *J. Phys. Chem.* **1992**, *96*, 5224. (c) White, H. S.; Peterson, J. D.; Cui, Q. Z.; Stevenson, K. J. *J. Phys. Chem. B* **1998**, *102*, 2930. (d) Smalley, J. F.; Chalfant, K.; Feldberg, S. W.; Nahir, T. M.; Bowden, E. F. *J. Phys. Chem. B* **1999**, *103*, 1676.

(25) (a) Hepel, M. In *Interfacial Electrochemistry: Theory, Experiments and Applications*; Wieckowski, A., Ed.; Marcel Dekker: New York, 1999; p 599. (b) Buttry, D. A.; Ward, M. D. *Chem. Rev.* **1992**, *92*, 1355.

(26) Luo, J.; Lou, Y. B.; Maye, M. M.; Zhong, C. J.; Hepel, M. *Electrochem. Commun.* **2001**, *3*, 172.

(27) (a) Soppimath, K. S.; Aminabhavi, T. M.; Kulkarni, A. R.; Rudzinski, W. E. *J. Controlled Release* **2001**, *70*, 1. (b) Hepel, M.; Mahdavi, F. *Microchem. J.* **1997**, *56*, 54.

(28) (a) Maye, M. M.; Zheng, W. X.; Leibowitz, F. L.; Ly, N. K.; Zhong, C. J. *Langmuir* **2000**, *16*, 490. (b) Maye, M. M.; Zhong, C. J. *J. Mater. Chem.* **2000**, *10*, 1895.

(29) Hepel, M.; Seymour, E.; Yogev, D.; Fendler, J. H. *Chem. Mater.* **1992**, *4*, 209.

(30) Hepel, M.; Zhang, X. M.; Stephenson, R.; Perkins, S. *Microchem. J.* **1997**, *56*, 79.

(31) Han, L.; Daniel, D. R.; Maye, M. M.; Zhong, C. J. *Anal. Chem.* **2001**, *73*, 4441.

(32) Kariuki, N.; Han, L.; Luo, J.; Zhong, C. J. Submitted to *Langmuir* for publication.

(33) Zhong, C. J.; Doblhofer, K. *Electrochim. Acta* **1990**, *35*, 1971.

(34) Maye, M. M.; Luo, J.; Han, L.; Zhong, C. J. *Nano Lett.* **2001**, *1*, 575.

(35) Hepel, M.; Chen, Y. M.; Stephenson, R. *J. Electrochem. Soc.* **1996**, *143*, 498.